

Chapter 2

EPITAXIAL SUPERCONDUCTORS ON ROLLING-ASSISTED-BIAXIALLY-TEXTURED-SUBSTRATES (RABiTS)

Amit Goyal

Metals and Ceramics Division
Oak Ridge National Laboratory
Oak Ridge, TN 37831
USA

2.1 INTRODUCTION

An overview of the fabrication of epitaxial, high- J_c , biaxially aligned YBCO thick films on Rolling-assisted-biaxially-textured-substrates (RABiTS) is provided. The RABiTS technique utilizes standard thermomechanical processing to obtain long lengths of flexible, biaxially oriented substrates with smooth surfaces (rms ~ 20 nm). The strong biaxial texture of the metal (in-plane $5\text{--}7^\circ$ FWHM) is conferred to the superconductor by deposition of intermediate metal and/or oxide layers which serve both as a chemical as well as a structural buffer. Epitaxial YBCO films have been grown using a variety of techniques on RABiTSTM with critical current densities exceeding 10^6 A/cm² at 77 K in self-field and have field dependences similar to that of epitaxial films on single crystal ceramic substrates. The texture of the base metal has been achieved in kilometer lengths and scaleable techniques are being pursued to deposit the epitaxial multilayers. Deposited conductors made using this technique offer a potential route for the fabrication of long lengths of high J_c wire capable of carrying high currents in high magnetic fields and at elevated temperatures.

2.2 BIAXIALLY TEXTURED METAL TEMPLATES

The formation of preferred orientations in metals as a result of cold work has been studied since the early 1920's and several books and reviews have been written on this subject (Barrett and Massalski, 1996). Advances within the last decade in understanding and representing orientations in three dimensions have allowed for significant understanding of deformation and annealing textures. Texture representation in

Euler (Bunge and Esling, 1982; Wenk and Kocks, 1987) and Frank Rodrigues (Frank, 1988) space is now commonly used to understand, predict and develop preferred orientation in metals and intermetallics. A recent overview article focusing on the advances within the last decade summarizes work to date on deformation and annealing textures in metals and intermetallics (Kad and Goyal, 1996). In the RABiTS process a metal or an alloy is first biaxially textured in long lengths by the processes of rolling and annealing (Goyal et al., 1996a, 1997; US Patents 5,739,086; 5,741,377; 5,846,912; 5,898,020). Substrates of interest for this application include cubic metals and alloys such as face-centered cubic (FCC) and body-centered cubic (BCC) materials. While BCC metals such as iron-based alloys could potentially be used, FCC metals and alloys are of primary interest for this application such as Ni and Cu based alloys. The only annealing texture in FCC metals that can be obtained in a single component as well as made to be very well-developed or sharp, is the cube texture. This texture corresponding to the orientation $\{100\}\{100\}$, consists of a cube plane parallel to the plane of the sheet and a cube edge parallel to the rolling direction. This is a unique texture, since it can be developed into an extremely sharp texture, unlike any other primary recrystallization texture in metals. A fully developed cube texture resembles a single crystal with a mosaic or subgrains. Silver as a metal to form biaxially textured templates has also been studied extensively because of its potential chemical compatibility with high temperature superconductors. However, due to the unique deformation characteristics of Ag at room temperature, it does not exhibit the standard Cu-type rolling texture upon heavy reduction via rolling. Modification of the stacking fault energy in Ag by rolling at higher temperatures close to 200°C permits the formation of the cube texture. Nevertheless, it is very difficult to obtain a “clean” texture in Ag because of the high tendency to form annealing twins. Even on the $\{100\}\{100\}$, cube textured Ag grains, two epitaxial orientations of most HTS materials are favored. Hence, a buffer layer is required between the Ag substrate and the superconductor layer. This defeats the purpose of using an expensive Ag substrate as the template. Moreover, at the commonly used temperatures for HTS deposition and buffer layer deposition, Ag has a very high vapor pressure. Hence, depositing on the Ag template is akin to depositing on high “mobile” surface. Most oxide films deposited on such substrates are therefore very rough and have textures which have a full-width-half-maximum (FWHM) substantially larger than the Ag substrate itself. Most of the work in this area has therefore focused on Ni and Cu based alloys.

Representative rolling textures of Ni-based substrates formed by consecutive rolling of a polycrystalline, randomly oriented bar to total deformations greater than 99%, followed by recrystallization are shown in Figure 2.1. Figure 2.1(a) and (b) show the (111), and (200) pole figures for an as-rolled Ni sample. This texture is referred to as the “Cu-Type” rolling texture. The localization of intensities along the $\{112\}\{111\}$ and the $\{123\}\{634\}$ orientations along the β -fiber or the skeleton line is evident when viewing the data in Euler space (Goyal et al., 1996b). By controlling the surface condition of the work rolls, it is possible to obtain substrates with surfaces as smooth as those obtained by mechanical and chemical polishing. Average line scans in $50\ \mu\text{m} \times 50\ \mu\text{m}$ region indicate a rms roughness of $\sim 10\ \text{nm}$ (Goyal et al., 1996b). The surface condition of a substrate can greatly affect epitaxy and integrity of buffer layers and hence the J_c of the superconducting film. Obtaining substrates with surfaces adequate for film growth without the need for a cumbersome polishing step is important for scale up to long lengths. Subsequent annealing of the substrates in a wide temperature range results in the formation of a sharp $\{100\}\{100\}$ cube texture. Figure 2.1(c) and (d) show the (111) and (200) pole figures for Ni recrystallized at 1000°C for 4 hrs in a vacuum of

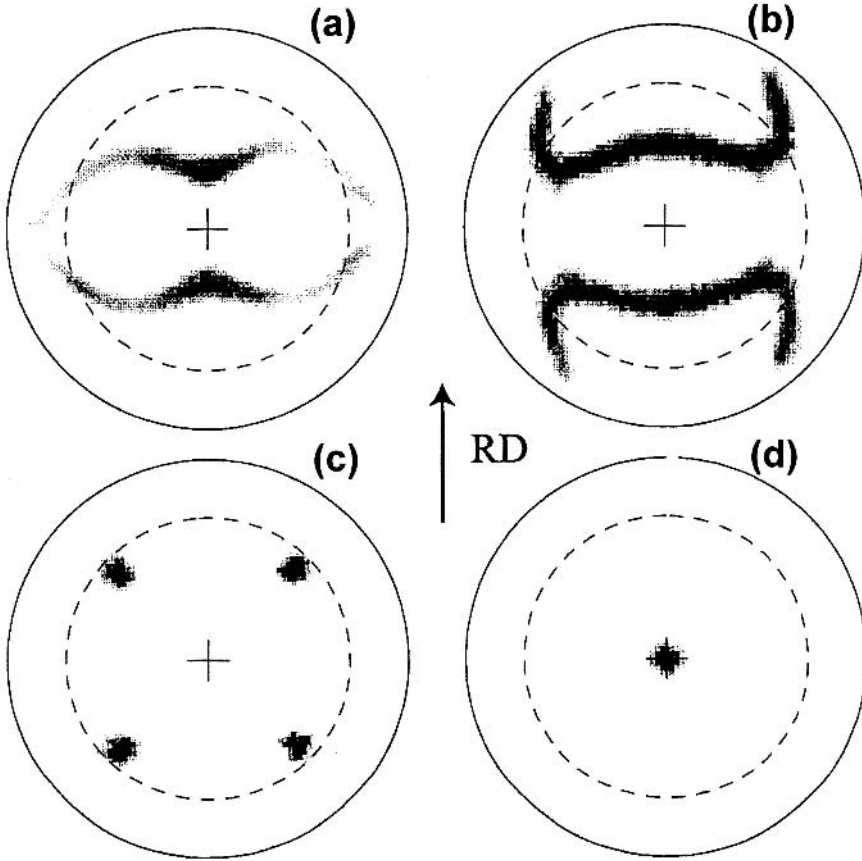


Figure 2.1. (a) Ni (111) pole figure and (b) Ni (200) pole figure of as-rolled substrate deformed greater than 99%. (c) Ni (111) pole figure and (d) Ni (200) pole figure of fully annealed substrate corresponding to figures (a) and (b).

$\sim 10^{-6}$ torr. The presence of a sharp, well-developed, single component cube texture is evident. Typical samples have X-ray ω - and ϕ -scans with full-width-half-maximum (FWHM) of 6° and 7° respectively. Depending upon the starting material, the impurity level and the deformation schedule, the cube texture can be made to be stable up to the melting point of Ni (Specht et al., 1998).

Figure 2.2 shows an orientation image micrograph of the Ni substrate. The micrograph was obtained using backscatter Kikuchi diffraction (BKD). Gray level shading on the micrograph is a reflection of the pattern quality or intensity of the Kikuchi bands observed at each point. Grain boundaries give rise to multiple diffraction patterns and hence have a poor pattern. Similarly, poor patterns are observed from any other crystallographic defect or strained region. BKD patterns were obtained on a hexagonal grid with a spacing of $3 \mu\text{m}$. The total number of patterns obtained in the $0.5 \mu\text{m} \times 0.5 \mu\text{m}$ region was close to 30,000. Indexing of the pattern at each location gave a unique measure of the orientation at that point. A hypothetical hexagonal lattice with a grain size of $3 \mu\text{m}$ was superimposed at each point from which a pattern was obtained. Grain boundary misorientations were then calculated for all the resulting boundaries using standard techniques. The micrograph was then regenerated with certain grain

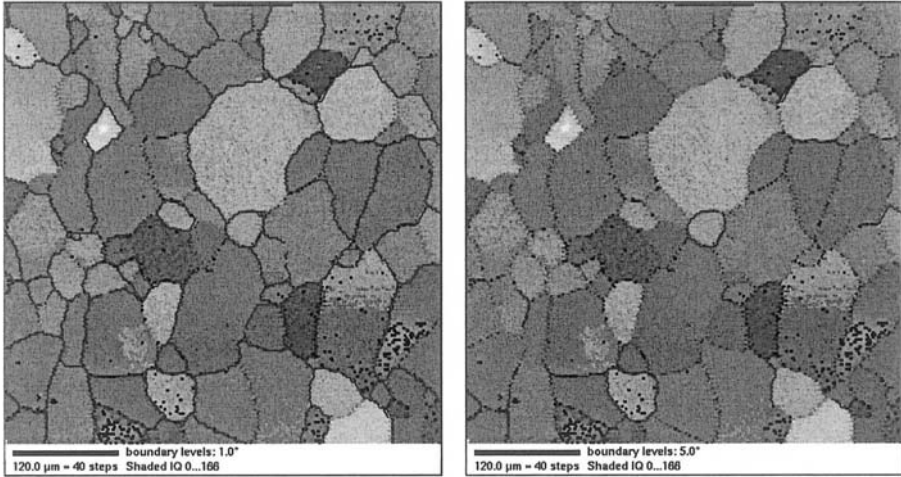


Figure 2.2. Electron backscatter Kikuchi diffraction created image of a macroscopic region of a cube textured Ni substrate. In Figure 2.2(a) and (b) all grain boundaries greater than 1° and 5° respectively are drawn.

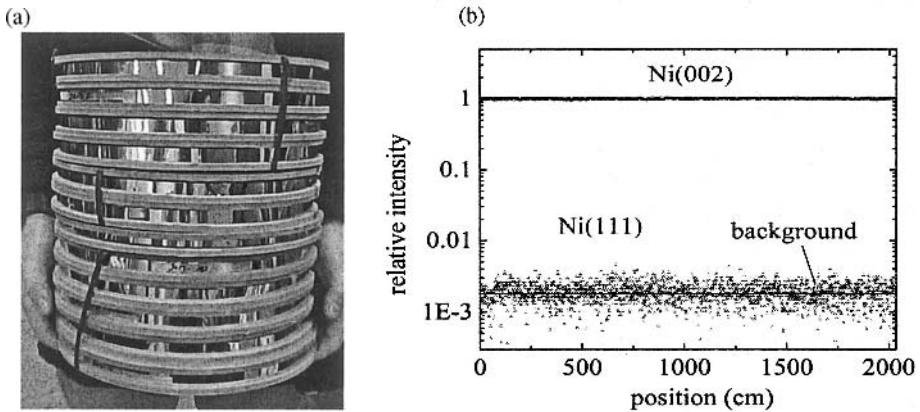


Figure 2.3. (a) Long lengths of heavily rolled Ni, 1 cm wide and $50\ \mu\text{m}$ thick Ni substrate which upon annealing at 1100°C for 1 h yields a sharp cube texture. (b) (002) and (111) X-ray peak intensities measured continuously along the length of a 20 m long cube-textured Ni substrate, 1 cm wide and $50\ \mu\text{m}$ thick. As can be seen, the (002) peak intensity is essentially constant along the length. The (111) peak intensity at all points is below the average background intensity.

boundary criteria. Figure 2.2(a) shows all grain boundaries greater than 1° and Figure 2.2(b) shows all grain boundaries greater than 5° . Substrates are typically textured in 4'' widths but widths greater than this are easily possible. Substrates have been fabricated in long lengths with piece lengths greater than 100 m. No technical limit on the length exists. Figure 2.3(a) shows 2 kilometers of textured Ni tape.

Figure 2.3(b) shows the (002) and (111) X-ray peak intensities measured continuously along the length of a 20 m long annealed Ni substrate, 1 cm wide and $50\ \mu\text{m}$ thick. A sharp cube texture and constant cube texture is evident from the high and constant peak intensity of the (200) peak. The (111) peak at all locations is in the background.

2.3 MACROSCOPIC TEXTURE CHARACTERIZATION OF BIAXIALLY TEXTURED SUBSTRATES

The degree of macroscopic texturing in a substrate is typically measured by X-ray diffraction. A pole figure gives a nice representation of the texture in the substrates. For example a Ni (111) pole figure is a representation of the orientation of the [111] direction of every Ni grain in the substrate. Figure 2.4(a) and (b) shows typical, background corrected, Ni (111) pole figures in linear scale. Only intensity close to the cube orientation, $\{100\}\langle 100\rangle$ is observed in these pole figures. In order to observe the texture quality more closely, Figure 2.4(c) and (d) show the corresponding background corrected, log-scale pole figures of the linear pole figures shown in Figure 2.4(a) and (b). It can clearly be observed that while the substrate corresponding to Figures 2.4(b) and (d) has a “clean” cube texture, the substrate corresponding to the pole figures shown in Figures 2.4(a) and (c) has other orientations present. Quantification of the % cube texture in the substrate is done by summing the intensities at the cube orientation locations divided by the total integrated intensity in the log-scale pole figure. For the substrate corresponding to Figure 2.4(b) and (d), the % cube texture is $\sim 100\%$, while

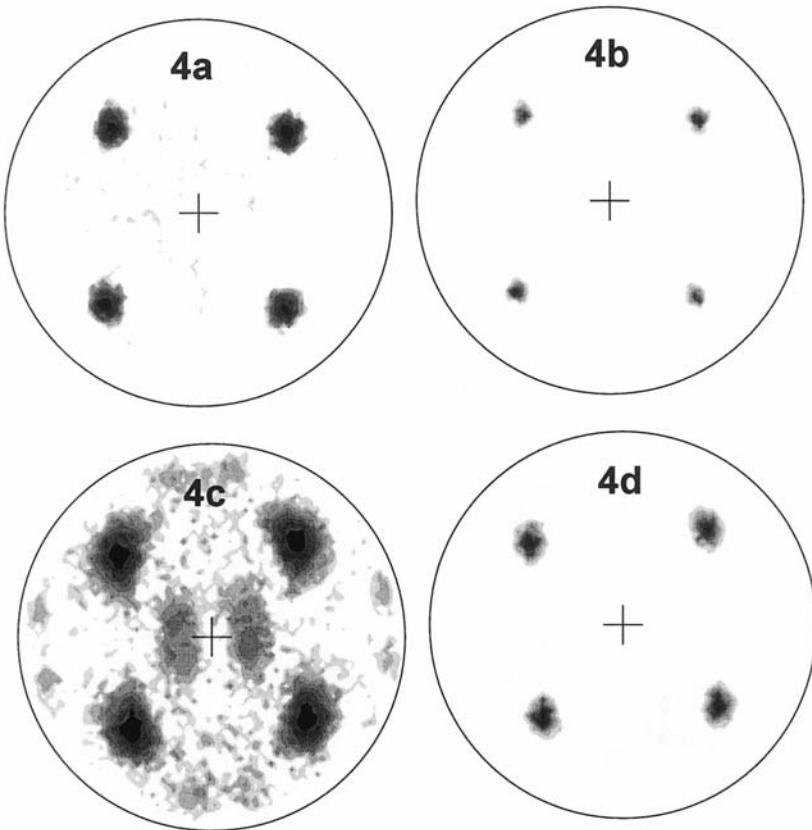


Figure 2.4. (a) and (b) Linear scale Ni (111) pole figures for two different substrates showing only cube poles; (c) and (d) Log-scale Ni (111) pole figures of the substrate corresponding to (a) and (b) respectively. It can clearly be seen that the substrate corresponding to figures (a) and (c) contains some retained rolling texture as well as twins.

that corresponding to Figure 2.4(a) and (c) is $\sim 94\%$. When the % cube texture is not close to 100%, numerous high angle grain boundaries can result in the substrate.

For determining the degree of in-plane and out-of-plane texture, omega-scans and phi-scans are done. The full-width-half-maximum (FWHM) of the out-of-plane texture is different for rocking about the rolling direction or in the direction. Typically the omega-scan is significantly broader for rocking about the rolling direction than for rocking in the rolling direction. Figures 2.5(a) and (b) show typical rocking curves in and about the rolling direction. The FWHM is determined by fitting a Gaussian to the experimentally measured data to avoid erroneous determinations due to outliers from few large grains in the sample. A typical phi-scan is shown in Figure 2.5(c). The FWHM is determined by averaging the FWHM of the four peaks shown in Figure 2.5(c).

Depending upon the starting grain size of the material before rolling, the degree of randomness of the starting texture and the rolling parameters, it is possible to obtain a substrate which shows no undesirable secondary recrystallization and maintains the primary recrystallization texture, i.e. the cube texture, till the melting point of the substrate. In such a case, significant sharpening of the out-of-plane and in-plane texture is possible by annealing at higher temperatures. Annealing at higher temperatures also reduces the twin density in the material. The grain size of the cube textured material continues to grow with annealing temperature but saturates when the substrate thickness is reached. Figure 2.6(a), (b) and (c) show the out-of-plane and in-plane texture, the corresponding twin density and grain size respectively of such a substrate as a function of the annealing temperature (Specht et al., 1998).

2.4 DEPOSITION OF THE SEED LAYER

Deposition of epitaxial buffer layers on textured metal or alloy substrates is a complex process because it involves the interaction between two surfaces with very different chemical properties. Under a wide range of deposition conditions for the oxide buffer layer, formation of NiO is favored. Typically this results in mixture of (111) NiO and (200) NiO. Even if a predominant (200) NiO is formed, the surface is quite rough. Hence, the deposition of oxide layers on metals and alloys of Ni and Cu is done under conditions where the formation of NiO or CuO is thermodynamically unfavorable. This is typically done by providing a background of 4% H₂ in argon or forming gas (Goyal et al., 1996a, 1996b, 1997; US Patents 5,739,086; 5,741,377; 5,846,912; 5,898,020; Norton et al., 1996; Paranthaman et al., 1997; He et al., 1997). If the deposition of the oxide layer is from a metal target such as during e-beam evaporation, a background of water of $\sim 1 \times 10^{-5}$ Torr is used to oxidize the material being deposited such as Ce (Paranthaman et al., 1997; He et al., 1997). Under these conditions, formation of a native metal oxide on the substrate, such as, NiO is thermodynamically unfavorable (Paranthaman et al., 1997; He et al., 1997).

Once oxidation of the Ni surface is prevented by choosing a seed layer that is thermodynamically more stable than NiO (e.g., CeO₂ or Y₂O₃-stabilized ZrO₂) and depositing it in reducing conditions, the lattice match between metal and oxide buffer layer is the main factor influencing epitaxial growth. This picture, however, is incomplete, since even under these conditions on many occasions, two in-plane epitaxial orientations of the seed oxide layer are observed. It is found that the presence of a fully developed $c(2 \times 2)$ sulfur superstructure on the surface of the Ni-alloy is essential for

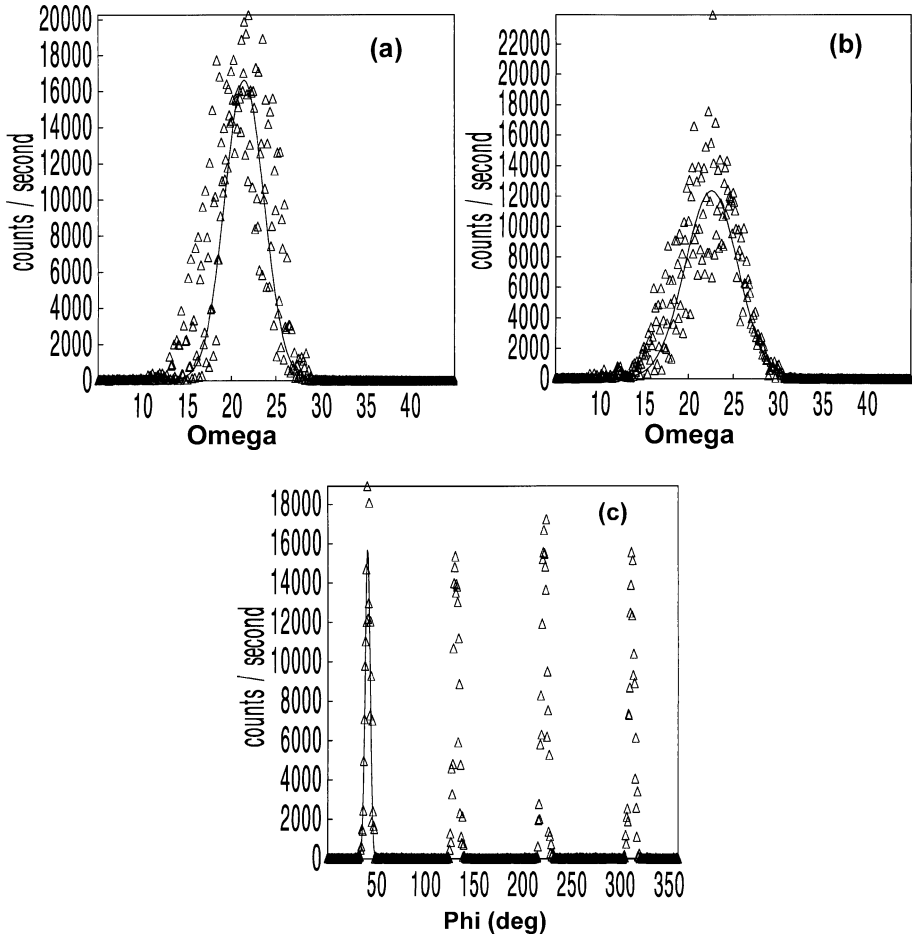


Figure 2.5. (a) Ni (200) Omega-scan or rocking curve when rocking *in*—the rolling direction. The fitted Gaussian to the data is used to obtain the full-width-half-maximum (FWHM) of the out-of-plane texture in the rolling direction; (b) Ni (200) Omega-scan or rocking curve when rocking *about*—the rolling direction. The fitted Gaussian to the data is used to obtain the full-width-half-maximum (FWHM) of the out-of-plane texture about the rolling direction, and (c) Ni (111) Phi-scan. The average FWHM obtained by fitting each of the four peaks by a Gaussian is used to obtain the full-width-half-maximum (FWHM) of the in-plane texture.

obtaining the correct epitaxial orientation of the seed layer (Cantoni et al., 2001, 2002, 2003). Figure 2.7(a) and (b) show *in-situ* reflection high energy electron diffraction patterns (RHEED) from the surface of a Ni with a $c(2 \times 2)$ superstructure and a Ni surface which has no $c(2 \times 2)$ superstructure (Cantoni et al., 2001, 2003).

Figure 2.8 shows the X-ray θ - 2θ patterns and relative pole figures acquired from the YSZ films grown on textured Ni with and without superstructure, respectively (Cantoni et al., 2001). The YSZ films were grown under the same conditions and with the same procedure, while monitoring the process with RHEED. The YSZ films grown on the $c(2 \times 2)$ surface showed single (002) orientation, with a (111) pole figure indicating the same degree of grain alignment as the substrate. The resulting YSZ unit cell was rotated 45° in plane with respect to the Ni cell, consistent with the ex-

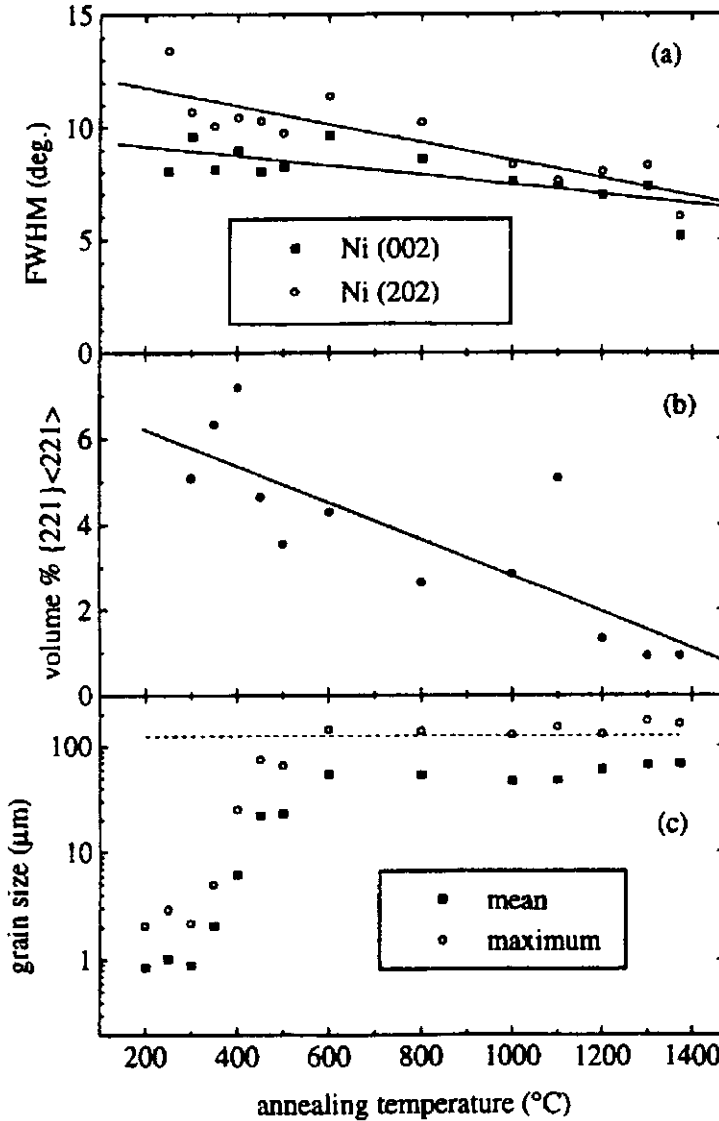


Figure 2.6. (a) FWHM of the omega and phi scan showing the out-of-plane and in-plane texture as a function of temperature; (b) volume % of twins in the substrate, and (c) grain size as a function of annealing temperature. The time at the annealing temperature was 10 mins for all temperatures studied.

pected cube-on-cube epitaxial orientation. In contrast, the YSZ films grown on the superstructure-free Ni overlayer showed only the (111) peak in the $\theta-2\theta$ scan. In this case, the pole figure of the (200) reflection showed 4 different in-plane domains rotated 30° with respect to each other. This epitaxial relation is expected for the nucleation of a threefold symmetric lattice on a square symmetric lattice.

From the above it is clear that the presence of the $c(2 \times 2)$ sulfur superstructure is essential for obtaining cube-on-cube epitaxy of oxide seed layers. The above analysis holds true for deposition of oxides with a fluorite structure (CeO_2 , YSZ, etc.),

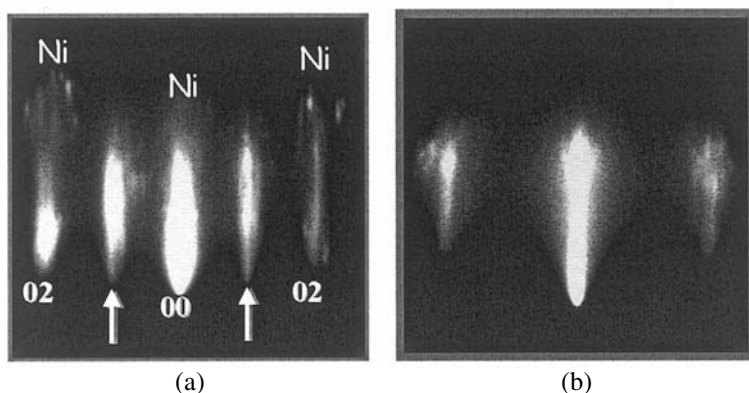


Figure 2.7. RHEED patterns obtained with the incident electron beam along $\langle 100 \rangle$ for: (a) RABiTS Ni and (b) Ni overlayer deposited by PLD on RABiTS Ni. The arrows in (a) indicate the existence of a $c(2 \times 2)$ superstructure that is absent in (b) (from Cantoni et al., 2001).

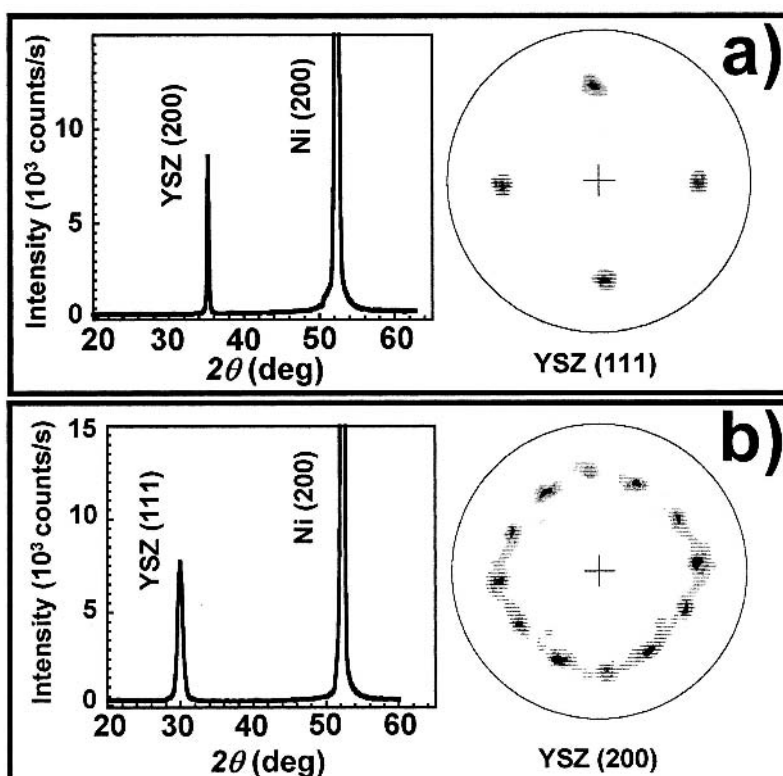


Figure 2.8. X-ray θ - 2θ scan and pole figure for: (a) the YSZ film grown on the $c(2 \times 2)$ superstructure present on RABiTS Ni and (b) the YSZ film grown on the Ni overlayer epitaxially deposited on RABiTS Ni without the sulfur superstructure (from Cantoni et al., 2001).

perovskite structure (such as SrTiO_3 , etc.), pyrochlore structure ($\text{La}_2\text{Zr}_2\text{O}_7$, etc.) and structure (Y_2O_3 , etc.) on Ni and Ni-alloy substrates. The effect of the sulfur super-

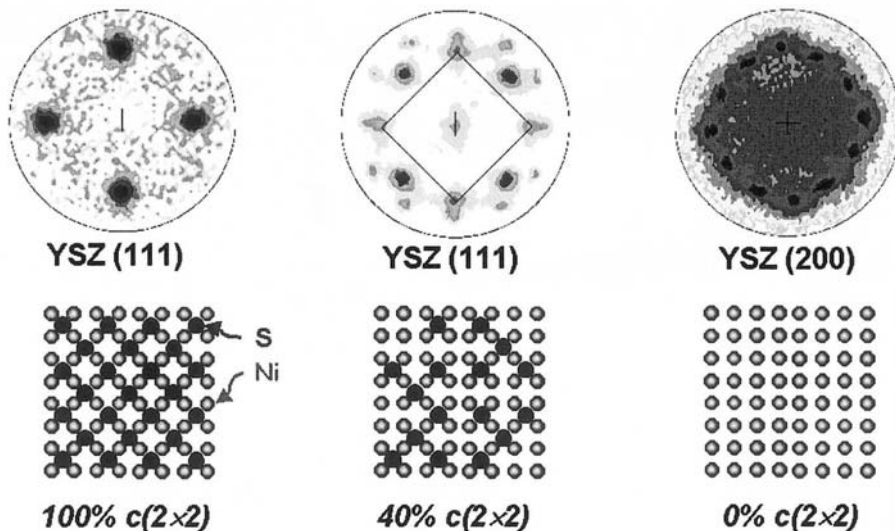


Figure 2.9. Comparison between pole figures of 3 different STO films grown on $\{100\}\langle 100\rangle$ Ni substrates having different sulfur coverage: 100% of a $c(2 \times 2)$ layer (0.5 ML) left; 40% middle; 0% right (from Cantoni et al., 2003).

structure has been explained on the basis of structural and chemical considerations. The S layer behaves like a template that well matches and mimics the arrangement of the oxygen atoms, in particular, the (001) sub-lattice planes for the seed layers mentioned above (Cantoni et al., 2001, 2002, 2003). Sulfur is chemically similar to oxygen and often exhibits the same electronic valence. The presence of such an ordered S template, thus, facilitates the bonding of the oxide cations in specific sites promoting the (001) epitaxial nucleation of the oxide film (Cantoni et al., 2001, 2002, 2003).

The $c(2 \times 2)$ sulfur superstructure can be formed on the surface of the Ni or Ni-alloy merely by surface segregation during the high temperature texture anneal (1000–1300°C) since sulfur is a common and almost unavoidable impurity in bulk Ni and Ni-alloys. However, depending upon the initial sulfur concentration in the metal or alloy as well as the specific texture annealing conditions, the sulfur superstructure can exhibit different coverage. The complete $c(2 \times 2)$ sulfur superstructure can be reproducibly formed on the surface of the metal/alloy tape by annealing the substrate at low temperatures (600–800°C) in very small amounts of H_2S (partial pressure of 1×10^{-7} to 1×10^{-6} Torr) for a few minutes (Cantoni et al., 2002, 2003). Previous surface studies have shown that H_2S molecules dissociate at the Ni surface and S atoms chemisorb forming a $c(2 \times 2)$ superstructure with a coverage that saturates to 0.5 ML corresponding to one complete atomic layer of the $c(2 \times 2)$ -S (Perdereau and Oudar, 1970; Andersson, 1976; Papageorgopoulos and Kamaratos, 1995). Incomplete $c(2 \times 2)$ superstructure results in mixed orientations of (200) and (111) textures of the oxide layer. Figure 2.8 shows comparisons between pole figures of YSZ films grown on cube textured Ni substrates having different sulfur coverages as determined by Auger Spectroscopy. In the first case, the substrate shows a complete S superstructure and the (111) logarithmic pole figure of the YSZ seed shows perfect cube texture. In the second case, the substrate superstructure exhibit a partial coverage ($\sim 40\%$) that translates to multiple orientation for the YSZ film. In the third case, the

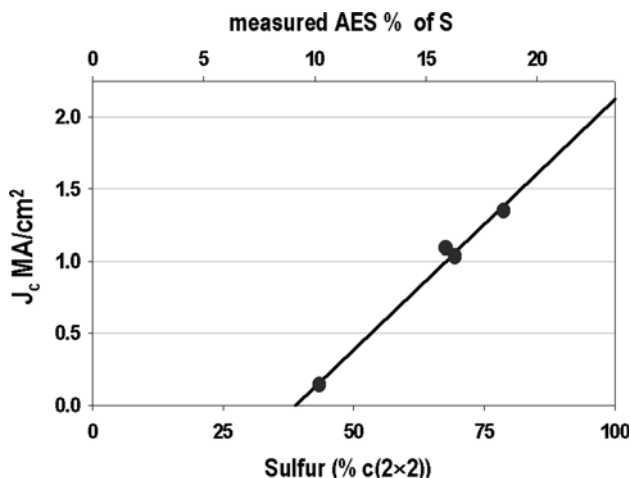


Figure 2.10. Critical current density versus initial substrate S concentration for four YBCO/CeO₂/YSZ/CeO₂/Ni RABiTS samples (from Cantoni et al., 2003).

surface of the substrate does not contain any S and the YSZ film shows only a (111) texture. In cases in which the substrate's S coverage was between 40 and 80% of a full $c(2 \times 2)$ layer, a cube texture with XRD peaks broader than those observed in seed layers grown on substrates with 100% $c(2 \times 2)$ were observed. The improvement in the texture of the seed layer determined by the S superstructure corresponds to an enhancement in J_c of the YBCO film subsequently deposited on the completed (seed plus buffer layer) RABiTS substrate.

This relation is illustrated in Figure 2.10, which plots the critical current density of 4 YBCO/CeO₂/YSZ/CeO₂/Ni samples versus the S surface content of the Ni substrate prior to seed layer deposition. The most commonly used seed layer at present is Y₂O₃. It is preferred over CeO₂ because it has a reduced tendency for cracking as well as reduced oxygen non-stoichiometry compared to CeO₂. Typical thickness of the seed layers in the range of 30–80 nm.

2.5 BARRIER AND CAP LAYER DEPOSITION

Once a high quality epitaxial seed oxide layer has been deposited, deposition of the barrier and cap layers is relatively straightforward. The most commonly used barrier layer for metal diffusion from the substrate to the superconductor layer is YSZ. Various techniques have been used to deposit the barrier layer. The important desired characteristic of the barrier layer besides texture is density. A dense layer is more effective in preventing metal diffusion to the superconductor layer. Pulsed laser ablation, rf-sputtering as well as reactive sputtering have been shown to result in dense YSZ layers. Typical thickness of the barrier layer is in the range of 150–300 nm depending on the time that will be required for deposition and/or formation of the superconductor layer during subsequent processing steps.

The most commonly used cap layer is CeO₂. Its purpose is to provide a good lattice match to YBCO. For growth of YBCO using the *ex-situ* BaF₂ process, CeO₂ is the only layer which results in good epitaxial growth of YBCO.

YBCO layer using in-situ deposition by PLD, MOCVD, CCVD or ex-situ deposition using the BaF ₂ or MOD TFA process
CAP Layer such as CeO ₂ , Y ₂ O ₃ , RE ₂ O ₃ , LaMnO ₃ , etc.
BARRIER Layer such as YSZ, RE ₂ O ₃ , LaMnO ₃ , etc.
SEED Layer such as CeO ₂ , Y ₂ O ₃ , RE ₂ O ₃ , La ₂ Zr ₂ O ₇ , SrTiO ₃ , LaMnO ₃ , LaNiO ₃ , TiN, etc.
Metal or Alloy substrate such as Ni, Ni-Cr, Ni-W, Ni-V, Ni-Cr-W, etc.

Figure 2.11. Various options for metal substrate, seed layer, barrier layer and cap layer that have been tried. It should be noted that for deposition of YBCO using the *ex-situ* BaF₂ process or the MOD TFA process, only the CeO₂ cap layer can be used.

Figure 2.11 shows a schematic of the buffer stack with the various options that have been tried for each layer in the stack.

Process parameters for deposition of barrier and cap layers via rf-sputtering have been published (List et al., 1988) and rf-sputtering is now routinely used to deposit these buffer layers in reel-to-reel configurations.

2.6 YBCO SUPERCONDUCTOR DEPOSITION

YBCO has been deposited on RABiTS substrates using pulsed laser ablation (PLD), metallorganic chemical vapor deposition (MOCVD) and the *ex-situ* BaF₂ process using e-beam co-evaporated precursors as well as using the metallorganic deposition (MOD) using the trifluoroacetate (TFA) process. In each case, high J_c 's have been reported exceeding 1 MA/cm² at 77 K, self-field. For short samples with YBCO deposition via PLD, J_c 's approaching 3 MA/cm² at 77 K, self-field has been obtained (Mathis et al., 1988).

In long lengths, fully buffered tapes coated with a single layer of YBCO precursor by a commercial web-coating process with MOD using a trifluoroacetate (TFA)-based precursor has been demonstrated (Verebelyi et al., 2003). The organic components were decomposed in a humid, oxygen atmosphere up to a temperature of 400°C, to form a BaF₂-based precursor film with stoichiometric Cu and Y oxides for YBCO. This precursor was continuously converted to the epitaxial superconducting phase in a tube furnace in a humid, low oxygen partial pressure environment (Verebelyi et al., 2003). The resulting film thickness was 1.0 μm measured by SEM cross-section analysis. The substrate used was a 75 μm thick NiW alloy with a buffer sequence of

Ni/Y₂O₃/YSZ/CeO₂. The Ni layer was 2 μm thick, the Y₂O₃ layer deposited by e-beam evaporation was 50 nm, the YSZ layer deposited by rf-sputtering was 300 nm thick and the CeO₂ also deposited by rf-sputtering was 30 nm thick. Figure 2.12 shows I_c at 77 K, self field, for two wires, A (7.5 m) and B (8.0 m), measured at 50 cm intervals using the standard 1 $\mu\text{V cm}^{-1}$ criterion. End-to-end I_c performance, also determined at a 1 $\mu\text{V cm}^{-1}$ criterion, was 132 and 127 A cm⁻¹ width for A and B, respectively. The inset in Figure 2.12 provides I_c statistical data for both wires. The 3.0 A cm⁻¹ width standard deviation (σ) of I_c , measured for wire A, is the highest uniformity yet reported on any second generation wire of this length. Wire B is a replicate of A with nearly the same I_c and only slightly higher variability. The higher variability translates to a smaller 'n value,' where n is the exponent of a power law fit to the end-to-end I - V curve near I_c , with wire B giving an exponent of 16 compared to 23 for wire A.

The chapter by Dominic et al. in this book covers details about *ex-situ* conversion of BaF₂ films.

Thick YBCO films have been grown on RABiTS substrates using PLD. Films of thickness 0.2–6.4 μm have been grown by PLD. Figure 2.13 shows the thickness dependence of J_c and I_c for YBCO films on two kinds of RABiTS substrates—Ni and Ni-3 at%W compared to the thickness dependence for YBCO on SrTiO₃ substrates by PLD (Kang et al., 2003).

The two kinds of RABiTS substrates correspond to Ni/CeO₂/YSZ/CeO₂ and Ni-3 at%W/Y₂O₃/YSZ/CeO₂. The Ni-3 at%W substrates were better significantly textured than Ni substrates. The NiW substrates are also significantly stronger than the Ni substrates and hence would have resulted in minimal damage during sample handling. Lastly, the presence of W, results in the formation of a NiWO₃ layer at the interface between NiW and NiO which restricts uncontrolled formation of NiO, thereby eliminating disruptions in the buffer stack (Leonard et al., 2003). The improved NiW substrates result in significantly better performance as indicated by the filled squares in Figure 2.13. The J_c is $\sim 0.8 \text{ MA/cm}^2$ at 77 K, self-field, even for a 4.3 μm thick YBCO film. Also included in this study was a 6.4 μm thick YBCO film on the substrate Ni-3 at%W/Y₂O₃/YSZ/CeO₂ which could not be characterized in transport due to the contacts opening up during the measurement (Kang et al., 2003; Leonard et al., 2003). Detailed examination of the texture by X-ray diffraction showed that texture did not degrade with thickness of the YBCO film. Transmission electron microscopy (TEM) showed that no dead layer of YBCO formed even for the 6.4 μm thick YBCO film. Figure 2.14 shows a collage of cross-section TEM images for the 6.4 μm thick film. As can be seen from the figure, no dead layer was formed. The YBCO film contains numerous defects such as stacking faults, dislocations and second phase particles of CuO and Y₂O₃ but uninterrupted c -axis growth can be seen throughout the thickness of the film (Leonard et al., 2003).

2.7 FABRICATION OF ALLOY SUBSTRATES

Various Ni-alloy substrates have been successfully cube textured via rolling and annealing (Goyal et al., 1999, 2000). As has been specified in these references, cube-textured alloys can be designed and fabricated such that their stacking fault frequency parameter, α , is less than 0.01 at deformations greater than 50%. The α can be determined by X-ray diffraction as outlined in reference 25 and 26. If α is greater than 0.01, then the composition can be modified such that α is less than 0.01. Once

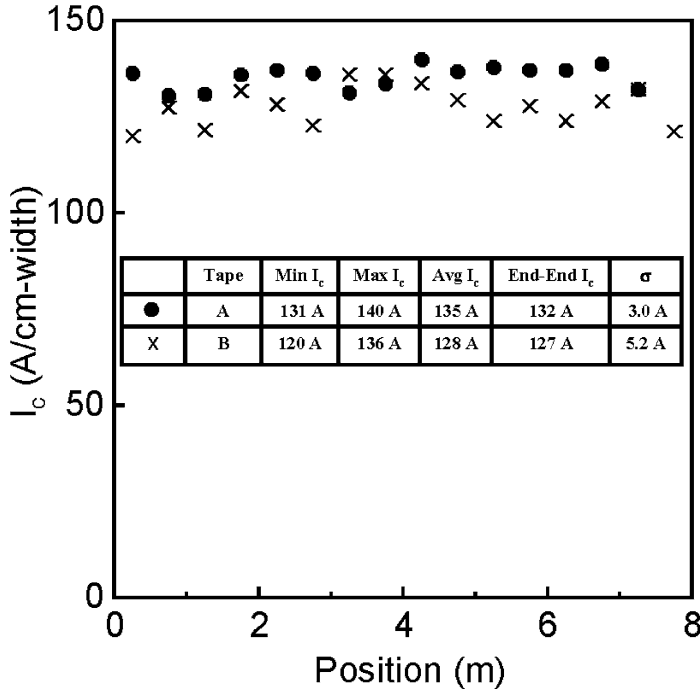


Figure 2.12. Critical current as a function of length, measured at 50 cm intervals, for two tapes, 7.5 m and 8 m long respectively at 77 K, self-field (from Verebelyi et al., 2003).

that is achieved the alloy can be rolled under conditions detailed below. If it is not possible to achieve α less than 0.01 at room temperature by compositional variation, then the rolling temperature can be increased to achieve it. The rolling then must be performed at this temperature. The rolling conditions in all cases are such that the total deformation is greater than 95%, the direction of rolling is preferably reversed at each pass and the annealing temperature is higher than the primary recrystallization temperature of the alloy. Using this method, single orientation, cube texture has been obtained in Ni–W alloys, Ni–Cr alloys, Ni–Mo alloys, Ni–V alloys, Ni–Cr–Al alloys and Ni–Cr–W alloys. Since cube textured NiW alloys were successfully developed (Goyal et al., 2002a), significant work has been performed in scaling these substrates up because of the ease of buffer layer deposition on these substrates. Tables 2.1 and 2.2 shows various binary and ternary substrates that have been cube-textured, indicating their %cube fraction, their yield strength in the annealed and textured state with the stress applied along the [100] crystallographic direction and their measured Curie temperatures. As can be seen from the figure, about 9 at%W and 13 at%Cr in binary alloys is required to get a completely non-magnetic substrate to minimize AC losses in application. Nevertheless, even lower alloying content substrates exhibit significantly reduced AC losses compared to a pure Ni substrate. As was shown in a study of Ni–Cr substrates with varying Cr contents, even small amounts of alloying element additions such as 7 at%Cr, result in significantly lower losses than that of pure Ni (Thompson et al., 2001). It is clear that there is significant world-wide interest in the fabrication of cube-textured, RABiTS alloy substrates (De Boer et al., 2001; Eickemeyer et al., 2001). For alloy substrates, in particular Ni-alloy substrates containing Cr, a trick is used to deposit high quality epitaxial buffer layers. Since deposition

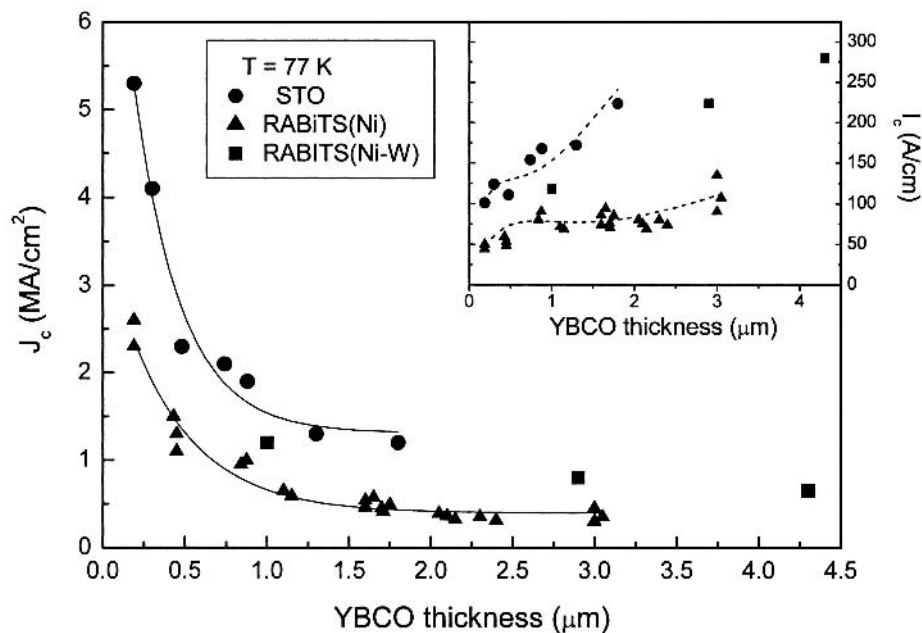


Figure 2.13. Critical current density as a function of YBCO film thickness on two kinds of RABiTS and STO substrates using PLD. Inset shows the critical current (A/cm-width).

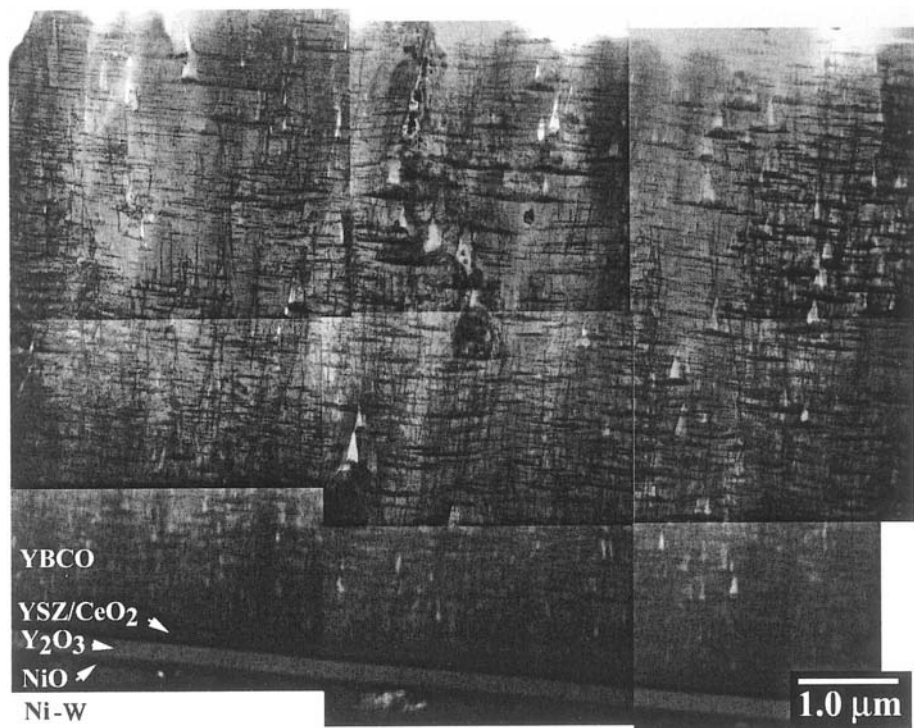


Figure 2.14. Composite cross-section image of the 6.4 μm thick YBCO film showing *c*-axis oriented growth throughout the full film thickness.

Table 2.1. Binary alloys of significant interest for use in RABiTS

Alloy	YS (0.2%)	Curie temp.
Ni	34 MPa	627 K
Ni-7 at%Cr	64 MPa	250 K
Ni-9 at%Cr	87 MPa	124 K
Ni-11 at%Cr	102 MPa	20 K
Ni-13 at%Cr	164 MPa	Non-magnetic
Ni-3 at%W	150 MPa	>400 K
Ni-5 at%W	165 MPa	335 K
Ni-6 at%W	197 MPa	?
Ni-9 at%W	270 MPa	~25 K

Table 2.2. Ternary alloys of significant interest for use in RABiTS

Ni-13 at%Cr-4 %Al	228 MPa	Non-magnetic
Ni-10 at%Cr-2 %W	150 MPa	Non-magnetic
Ni-8 at%Cr-4 at%W	202 MPa	Non-magnetic

of epitaxial oxides directly on the Cr containing alloy results in the formation of undesirable Cr_2O_3 , a Ni overlayer or a Ni–W overlayer is first deposited epitaxially on the Ni–Cr alloy substrate (Goyal et al., 2002c). Using this process, J_c 's over 1 MA/cm^2 in self-field, 77 K have been demonstrated (Goyal et al., 2002c).

Significant interest is currently in making alloy substrates using powder metallurgy as a route to making the starting coil (Goyal et al., 2001, 2002b, 2003). Powder metallurgy allows fabrication of alloys with homogeneous compositions without the detrimental effects of compositional segregation commonly encountered when using vacuum melting or casting to make alloys. Furthermore, powder metallurgy allows easy control of the grain size of the starting alloy body. Moreover, powder metallurgy allows a fine and homogeneous grain size to be achieved. Most importantly, using powder metallurgy, starting coils can be directly obtained at the desired thickness using well developed industry procedures without the need for complicated hot-rolling to homogenize the material with respect to grain size as is required for vacuum melted ingots. Using powder metallurgy, long lengths, over 2 km of Ni-3 at%W substrates have been fabricated by ORNL (Goyal et al., 2002a). Efforts are currently underway to fabricate Ni-5 and 9 at%W substrates via the powder metallurgy route.

An important point to mention is that AC losses from a substrate which is magnetic depends on the defect density in the substrate. Losses are an extrinsic feature and the Curie temperature is an intrinsic property of the substrate, much like the critical current density is an extrinsic property of the superconductor and depends upon defects while the superconducting transition temperature is an intrinsic property. Hence, depending on how a low alloying element substrate which is magnetic will contribute to losses depends on how the substrate has been handled after the final high temperature texture recrystallization anneal.

Two additional methods exist to fabricate highly textured alloy substrates which reduced magnetism and have high mechanical strength. Both approaches are composite approaches to make substrates. In the first approach (Goyal et al., 2002) a powder-in-tube method using a Ni or Ni-alloy tube filled with non-magnetic and mechanically strong alloy powder or rod is heavily deformed followed by annealing. The result is cube-textured exterior and an un-textured interior. Alternatively, a rod of a hard, non-

magnetic but deformable alloy is coated with Ni or a Ni-alloy which can result in the formation of a cube texture, is heavily deformed and annealed to form a textured exterior and an un-textured interior. In the second approach, a rolled substrate of a composition which can be cube textured is laminated in the final step with a mechanically strong and non-magnetic substrate (Goyal et al., 2000).

2.8 SUMMARY

The rolling-assisted-biaxially-textured-substrates (RABiTS) as shown schematically in Figure 2.15 appears to be a promising and industrially scalable method to fabricate long-lengths of high performance superconductors. Using this method, critical current densities exceeding 3 MA/cm^2 have been demonstrated for YBCO films. I_c /width approaching 300 A/cm width in thick films have also been demonstrated. Most importantly, reel-to-reel, continuously fabricated epitaxial YBCO/RABiTS have J_c 's over 1 MA/cm^2 and I_c 's of $\sim 130 \text{ A}$ in 8 meter long lengths, showing the viability of this process. Efforts are presently underway world-wide to achieve large-scale manufacturing of high performance and low-cost conductors using this process.

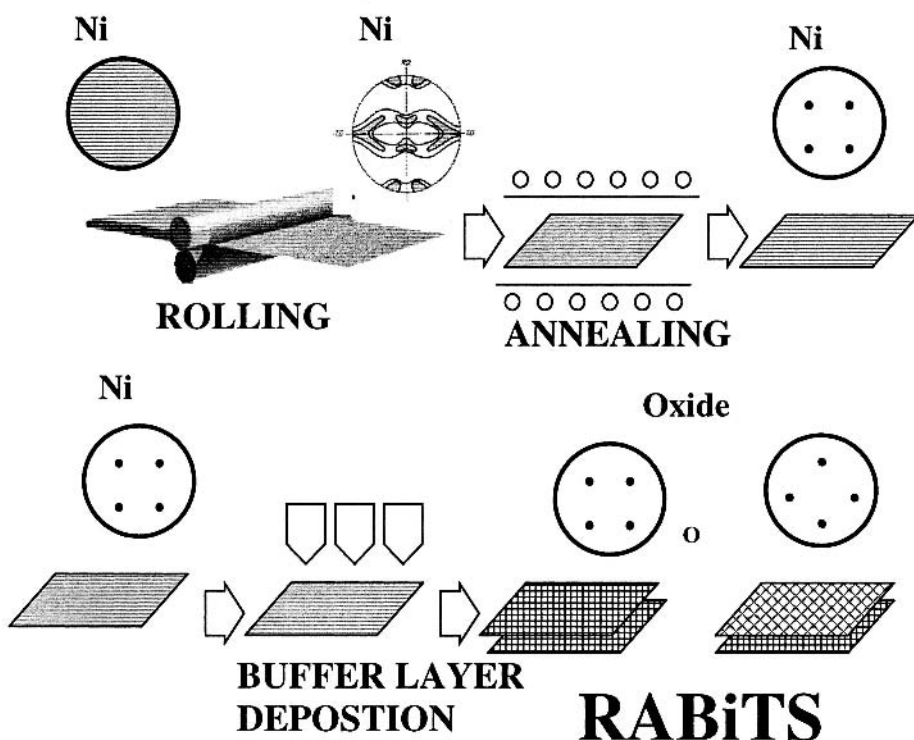


Figure 2.15. Schematic of the RABiTS process. First an untextured metal alloy is rolled to produce a particular desired rolling texture which upon annealing results in a sharp cube texture. Epitaxial buffer layers comprising generally of a seed layer, a barrier layer and a cap layer are then epitaxially deposited on the cube textured metal/alloy substrate. This comprises the **Rolling-Assisted-Biaxially-Textured-Substrates** (RABiTS) process. Epitaxial superconductors such as YBCO is then epitaxial deposited or formed on the substrate.

REFERENCES

- Andersson, S., 1976, *J. Phys. C*, 9:2721.
- Barrett, C.S. and Massalski, T.B., 1996, *Structure of Metals*, McGraw-Hill, New York.
- Bunge, H.J. and Esling, C., 1982, *Quantative Texture Analysis*, Dgm, Oberursel.
- Cantoni, C., Christen, D.K., Feenstra, R., Norton, D.P., Goyal, A., Ownbyand, G.W., and Zehener, D.M., 2001, *Appl. Phys. Lett.*, 79:3077.
- Cantoni, C., Christen, D.K., Heatherly, L., Kowalewski, M.M., List, F.A., Goyal, A., Ownby, G.W., Zehner, D.M., Kang, B.W., and Kroeger, D.M., 2002, *J. Mat. Res.*, 17:2549–2554.
- Cantoni, C., Christen, D.K., Goyal, A., Heatherly, L., List, F.A., Ownby, G.W., Zehner, D.M., Christen, H.M., and Rouleau, C.M., 2003, *IEEE Trans. Appl. Supercond.*, 13:2646–2650.
- De Boer, B., Eickemeyer, J., Reger, N., Fernandez, G.R., Ritcher, J., Holzapfel, B., Schultz, L., Prussiet, W., and Berberich, P., 2001, *Acta Met.*, 49:1421.
- Eickemeyer, J., Selbmann, D., Opitz, R., De Boer, B., Holzapfel, B., Schultz, L., and Miller, U., 2001, *Supercond. Sci Technol.*, 14:152.
- Frank, F.C., 1988, *Met. Trans.*, 19A:403.
- Goyal, A., 2001, US Patent 6,180,570, January 30.
- Goyal, A., 2002, US Patent 6,375,768, April 23.
- Goyal, A., Norton, D.P., Budai, J.D. et al., 1996a, *Appl. Phys. Lett.*, 69(12):1795.
- Goyal, A. et al., 1996b, *Appl. Supercond.*, 4:403–427.
- Goyal, A. et al., 1997, *J. Mater. Res.*, 12:2924–2940.
- Goyal, A. et al., 1999, US Patent 5,964,966, October 12.
- Goyal, A. et al., 2000, US Patent 6,106,615, August 22.
- Goyal, A. et al., 2001, US Patent 6,331,199, December 18.
- Goyal, A. et al., 2002a, *Physica C*, 382:251.
- Goyal, A. et al., 2002b, US Patent 6,447,714, September 10.
- Goyal, A. et al., 2002c, US Patent 6,451,450, September 17.
- Goyal, A. et al., 2003, US Patents 6,599,346, July 29; 6,602,313, August 5; 6,602,313, August 5; 6,607,838, August 19; 6,607,839, August 19; 6,610,413, August 26; 6,610,414, August 26; 6,635,097, October 21.
- He, Q., Christen, D.K. et al., 1997, *Physica C*, 275:155.
- Kad, B. and Goyal, A., 1996, Metals Information Analysis Center (MAIC), Report No. 9.
- Kang, S., Goyal, A., Leonard, K.J., Rutter, N.A., and Kroeger, D.M., 2003, *J. American Ceramic Society* (submitted for publication).
- Leonard, K.J., Kang, S., Goyal, A., Thomas, K.A., and Kroeger, D.M., 2003, *J. Mater. Res.*, 18:1723–1732.
- List, F.A., Goyal, A., Paranthaman, M., Norton, D.P., Specht, E.D., Lee, D.F., and Kroeger, D.M., 1988, *Physica C*, 302:87–92.
- Mathis, J.E., Goyal, A., Lee, D.F., List, F.A., Paranthaman, M., Christen, D.K., Specht, E.D., Kroeger, D.M., and Martin, P.M., 1988, *Jpn. J. Appl. Phys., Part 2—Letters*, 11B:L1379–L1382.
- Norton, D.P., Goyal, A., Budai, J.D. et al., 1996, *Science*, 274:755.
- Papageorgopoulos, C.A. and Kamaratos, M., 1995, *Surf. Sci.*, 338:77.
- Paranthaman, M., Goyal, A., List, F.A. et al., 1997, *Physica C*, 231:266.
- Perdereau, M. and Oudar, J., 1970, *Surf. Sci.*, 20:80.
- Specht, E.D., Goyal, A., Lee, D.F., List, F.A., Kroeger, D.M., Paranthaman, M., Williams, R.K., and Christen, D.K., 1998, *Supercond. Sci. Technol.*, 11:945–949.
- Thompson, J.R., Goyal, A., Christen, D.K., and Kroeger, D.M., 2001, *Physica C*, 370:169.
- Verebelyi, D.T., Schoop, U., Thieme, C., Li, X., Zhang, W., Kodenkandath, T., Malozemoff, A.P., Nguyen, N., Siegal, E., Buczek, D., Lynch, J., Scudiere, J., Rupich, M., Goyal, A., Specht, E.D., Martin, P., and Paranthaman, M., 2003, *Supercond. Sci. Technol.*, 16:L19–L22.
- Wenk, H.R. and Kocks, U.F., 1987, *Met. Trans.*, 18A:1083.



<http://www.springer.com/978-1-4020-8117-0>

Second-Generation HTS Conductors

Goyal, A. (Ed.)

2005, XVIII, 347 p., Hardcover

ISBN: 978-1-4020-8117-0